



Article

Kinematic Rupture Process and Its Implication of a Thrust and Strike-Slip Multi-Fault during the 2021 Haiti Earthquake

Guisen Wen 1, Xingxing Li 1,*, Yingwen Zhao 1, Yong Zhang 2, Caijun Xu 1 and Yuxin Zheng 1

- ¹ School of Geodesy and Geomatics, Wuhan University, Wuhan 430079, China
- ² School of Earth and Space Sciences, Peking University, Beijing 100871, China
- * Correspondence: xxli@sgg.whu.edu.cn

Abstract: A devasting Mw7.2 earthquake struck southern Haiti on 14 August 2021, leading to over 2000 casualties and severe structural failures. This earthquake, which ruptured ~70 km west of the 2010 Mw7.0 event, offers a rare opportunity to probe the mechanical properties of southern Haiti. This study investigates the kinematic multi-fault coseismic rupture process by jointly analyzing teleseismic and interferometric synthetic aperture radar (InSAR) datasets. We determined the optimal dip of different segment faults through finite-fault inversion, and the results show that the dips of the first, second and third faults are 62°, 76° and 76°, respectively, coinciding with the relocated aftershock distribution. The results estimated from our joint inversion revealed that the slip was dominated by reverse motion in the first segment and strike-slip motion in the second and third segments. Three slip patches were detected along the strike, with a peak slip of 3.0 m, and the rupture reached the surface at the second segment. The kinematic rupture process shows a unilateral rupture with a high centroid rupture velocity (5.5 km/s), and the rupture broke through the stepover and caused a cascade rupture. The rupture front experiences a directivity pulse of high ground motions with high amplitude and short duration, which may be an additional factor explaining the many landslides concentrated on the western end of the fault. The Coulomb failure stress change result indicates the increases in the probability of future events to the east and west of the 2021 main shock.

Keywords: joint inversion; multi-fault segment; cascade rupture; unilateral propagation



Citation: Wen, G.; Li, X.; Zhao, Y.; Zhang, Y.; Xu, C.; Zheng, Y. Kinematic Rupture Process and Its Implication of a Thrust and Strike-Slip Multi-Fault during the 2021 Haiti Earthquake. *Remote Sens.* 2023, *15*, 1730. https://doi.org/ 10.3390/rs15071730

Academic Editor: Salvatore Stramondo

Received: 11 February 2023 Revised: 19 March 2023 Accepted: 20 March 2023 Published: 23 March 2023



Copyright: © 2023 by the authors. Licensee MDPI, Basel, Switzerland. This article is an open access article distributed under the terms and conditions of the Creative Commons Attribution (CC BY) license (https://creativecommons.org/licenses/by/4.0/).

1. Introduction

On 14 August 2021, a devasting Mw7.2 earthquake struck southern Haiti (Figure 1), causing over 2000 deaths, 13,000 injury casualties, destruction of at least 140,000 houses, and severe infrastructural damage [1]. The Caribbean and North American plates converge obliquely at ~20 mm/year (Figure 1a) [2–5]. The plate motions are largely accommodated by the Septentrional fault zone and Enriquillo-Plantain Garden (EPG) strike-slip fault zones [6,7], forming the intermediate Gonave microplate. Haiti is located on a tectonic boundary between the Caribbean plate and the Gonave microplate and has long been recognized as an active tectonic region. The observations revealed that the plate motion between the Caribbean and Gonave microplates is accommodated by ~6 mm/yr and 9 ± 3 mm/yr of sinistral slip [3] and reverse slip [8], respectively. Such a tectonic setting leads to a complex fault system and earthquake rupture mode.

Historical earthquake studies show that southern Haiti was struck by several significant earthquakes (i.e., 1701, 1751, 1770 and 1860) [9–11]. The investigation of 2010 Mw7.0 and 2021 Mw7.2 events which were observed by modern instrumental data, have provided profound insights into the fault system and seismic activity in the southern Haiti region. Previous investigation shows that the 2010 earthquake did not rupture the EPG fault but two neighboring faults [12,13], and the rupture mode changed from thrust and strike-slip motion. The 2021 Mw7.2 Haiti earthquake occurred in an area ~70 km west of the 2010 event; the impact was much lower than the 2010 Mw7.0 event because the area

Remote Sens. 2023, 15, 1730 2 of 16

of the 2021 Haiti earthquake is mostly rural, with a low population density [2,12–15]. The U.S. Geological Survey (USGS) National Earthquake Information Center (NEIC) reported that the 2021 Haiti earthquake occurred at 18.434°N, 73.482°W, and on 14 August 2021 12:29:08 (UTC). Moment tensor solutions from USGS and Global Centroid Moment Tensor (GCMT) suggest the 2021 Haiti earthquake was an oblique left-lateral thrust event. The interferometric synthetic aperture radar (InSAR) shows substantial vertical motion [16,17] near the epicenter and the north of the EPG fault, and the coseismic deformation reached the surface at ~40 km west of the epicenter. The crustal deformation suggests that the 2021 Haiti earthquake ruptured a multi-fault system, and the fault geometry of this earthquake seems to not align with the EPG fault [18,19]. Given the historic earthquake and the tectonic setting in Haiti, studying the seismogenic mechanism of the Haiti earthquake is valuable for better understanding the regional mechanical properties with strong earthquake activity.

Several authors have studied the source characteristics of the 2021 Haiti earthquake utilizing seismic and/or geodetic datasets [18–21]. Relocated aftershock distribution delineates three north-dipping structures located north of the EPG fault [21], providing a reference for fault geometries. Okuwaki and Fan (2022) obtained a finite-fault model with two slip patches that combine thrust and strike-slip motion, using the teleseismic P wave [18]. The slip patches separate ~70 km due to the low spatial resolution of the teleseismic data, which is different from the InSAR observation. To better illustrate the fault model, Maurer et al. (2022) generated fault geometries from an updated fault database for finite-fault inversion [19]. They argued that the earthquake started with a reverse slip on the EPG fault near the hypocenter and jumped the restraining bend in the EPPG fault near Pic Macaya, with a left-lateral slip. Calais et al. (2022) solved two fault models through a non-linear least squares search method and a coseismic slip model using InSAR data [20]. The main characteristics of the finite-fault inversion results from previous studies revealed two slip patches; the first slip patch is located near the hypocenter with primarily reverse motion, and the second is located at the west of the epicenter with primarily left-lateral motion [18–20]. However, the finite-fault models derived using a single dataset are constrained to the sparse spatial or temporal resolution, with which it is difficult to represent the detailed rupture characteristics. Up to now, there is no research about the joint inversion with geodetic deformation and seismic waves in the finite-fault rupture process of the 2021 Haiti earthquake. Therefore, it is significant to determine the fault geometry and obtain a rupture process model that simultaneously explains the teleseismic and InSAR data. Additionally, a high spatiotemporal resolution fault model contributes to understanding the rupture evolution of the 2021 Haiti earthquake.

In this study, we investigate the rupture process of the 2021 Haiti earthquake by jointly analyzing teleseismic and InSAR datasets, and the Coulomb stress-related triggering relationship between this event and its peripheral fault zone based on the finite-fault rupture process model. Our principal scientific objective is to delineate the kinematic rupture process evolution of the 2021 Mw7.2 Haiti earthquake and to obtain basic knowledge about the mechanical response following the event. Therefore, the main work process of this study is as follows: (1) We determined the optimal fault geometry strikes and dips using the grid-search method and inverted the coseismic rupture model by joining the teleseismic and InSAR data. The results show that the 2021 Haiti earthquake combines the thrust and strike-slip motion and the dips in the thrust and strike-slip fault have changed ~14°. (2) We calculated the Coulomb failure stress change (Δ CFS) through the joint finite-fault model. (3) We explored the implications of our results.

Remote Sens. 2023, 15, 1730 3 of 16

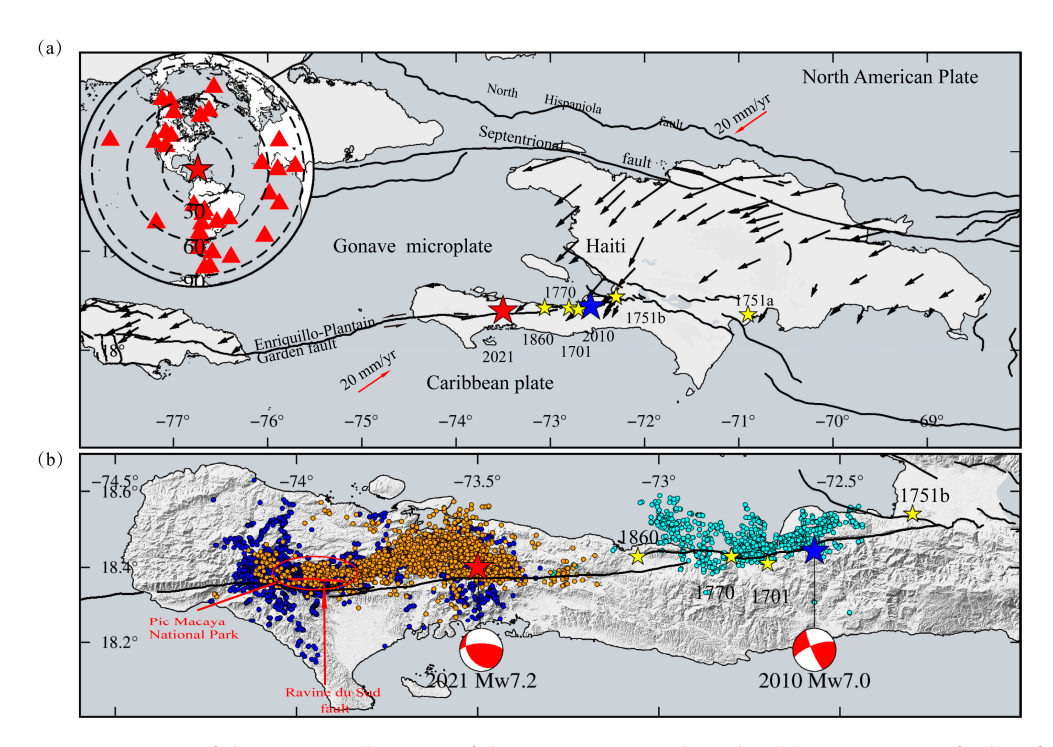


Figure 1. Map of the epicentral region of the 2021 Haiti earthquake. (a) Major active faults of the Caribbean–North America plate boundary zone [22,23]. The red, blue and yellow stars denote the epicenter location of 2021, 2010 and historic earthquakes (i.e., 1701, 1751a, 1751b, 1770 and 1860). Black arrows denote the Global Positioning System (GPS) velocities [3]. The inset at the upperleft corner shows the 32 teleseismic stations (red triangles) and the epicenter (red star) of the 2021 Haiti earthquake. (b) The orange dots denote the relocated aftershock catalogs from 20 August to 31 December 2021 [21]; the cyan dots denote the relocated aftershock catalogs after the 2010 main shock [14]; and the blue dots denote the landslide distribution [24]. The red ellipse in (b) denotes the Pic Macaya National Park, and the red line denotes the Ravine du Sud fault.

2. Materials

To better understand the rupture history and assess the hazards of the 2021 Haiti earthquake, we use the teleseismic data and InSAR data to image the earthquake rupture process. We downloaded the teleseismic wave from the Incorporated Research Institutions for Seismology (IRIS) data center. We considered the teleseismic stations with epicentral distances between 30° and 90° and selected 32 vertical components of teleseismic P waves to ensure good coverage of both azimuthal and take-off angles over the epicenter (inset in Figure 1a). The raw data were resampled to 1 sample per second, and the duration is 60 s. We integrated original velocity seismograms into displacement waves and then bandpass-filtered to 0.01–0.2 Hz.

We also obtained the surface line-of-sight (LOS) displacements from the Sentinel-1 (T004A and T142D) and ALOS-2 (T042A, T043A and T138D) data [16,17]. The LOS displacements of these five tracks are shown in Figure S1. Finally, 507, 364, 570, 612 and 507 data points were downsampled from the T004A, T042A, T043A, T138D and T142D datasets, respectively, using a quadtree sampling algorithm [25].

3. Inversion and Results

3.1. Finite-Fault Inversion

This study uses a linear inversion method to determine the finite-fault rupture model [26]. In the rupture process inversion, the subfault source time functions (STFs) were modeled in a linear way [27], and the rake of each subfault can be estimated simultaneously. The joint inversion can be expressed as

Remote Sens. 2023, 15, 1730 4 of 16

$$\begin{bmatrix} \lambda_1 \mathbf{U}_1 \\ \lambda_2 \mathbf{U}_2 \\ 0 \\ 0 \\ 0 \end{bmatrix} = \begin{bmatrix} \lambda_1 \begin{bmatrix} G_x & G_y \end{bmatrix} \\ \lambda_2 \begin{bmatrix} Q_x & Q_y \end{bmatrix} \\ \lambda_{II} \mathbf{D} \\ \lambda_{III} \mathbf{T} \\ \lambda_{III} \mathbf{Z} \end{bmatrix} \begin{bmatrix} \mathbf{m}_x \\ \mathbf{m}_y \end{bmatrix}$$
(1)

where U_1 and U_2 denote the observation of waveform and InSAR data; G_x , G_y and Q_x , Q_y denote the Green's function of waveform and InSAR data; m_x and m_y represent the slip rate amplitudes of all subfaults; λ_1 , λ_2 denote the relative weight of waveforms and InSAR data; D, T, Z denote the matrix of the spatial, temporal smoothness and minimization scalar moment constraints; and λ_I , λ_{III} , are the corresponding weights of constraints. The conjugate gradient least-squares method is used to solve this inversion equation, and we can obtain the final results after the iterations.

In the joint inversion, we used the code "QSSP" [28] to calculate the Green's functions for teleseismic data based on the AK135 model [29], and used the software "PSGRN" [30] to calculate the Green's functions for InSAR data. We assumed a total rupture duration of 35 s in inversion, which means the rupture window of each subfault lies in 0-35 s. This time duration was chosen by considering that (1) the half-duration time of centroid moment tensor solution is 9 s and 16 s, respectively, from GCMT and USGS; and (2) previous studies [18,20] (e.g., Calais et al., 2022; Okuwaki and Fan, 2022) showed the rupture durations are about 30 s. Additionally, we used a maximum rupture velocity and a maximum duration time to limit the subfault rupture window to stabilize the inversion. In principle, we preferred a narrow time that improves the calculated efficiency and generates a small-enough misfit. Finally, we used a maximum rupture velocity of 3.2 km/s and a duration of 8 s in inversion according to the relative misfit curve (Figure 2), which means that the rupture velocity can range between d/(d/3.2 + 8) and 3.2 km/s for a subfault d km away from the rupture initiation [27,31]. Additionally, spatial, and temporal smoothness and minimizing scalar moment constraints were introduced to stabilize the ill-posed problem in the inversion of the rupture process [26]. The weights of 300, 1 and 0.5 were chosen using the trial-and-error method to ensure a small-enough relative misfit between the observed and that synthetic data and the inversion results (i.e., moment-rate function and slip distribution) change smoothly.

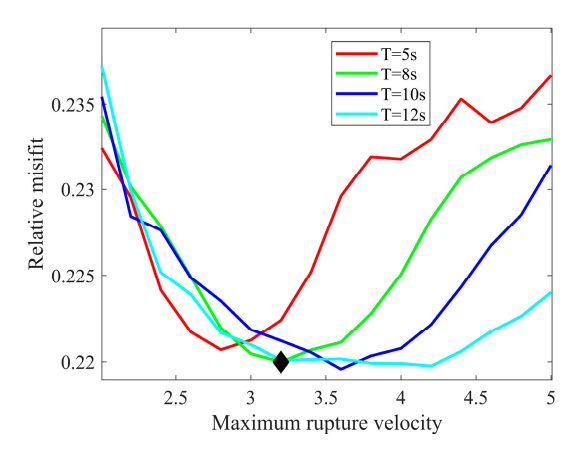


Figure 2. Relative misfit curve with different maximum rupture velocities (changes from 2 to 5 km/s) and maximum rupture duration time of 5 s (red), 8 s (green), 10 s (blue) and 12 s (cyan) of each subfault. We prefer a maximum rupture velocity of 3.2 km/s and a maximum rupture duration of 8 s for each subfault in this study (black diamond).

The teleseismic and InSAR data were normalized by their vector L^2 -norm (i.e., $u^{obs} = \frac{u^{obs_ori}}{\sqrt{\sum_n (u^{obs_ori}(n))^2}}$; u^{obs} is the normalized data, and u^{obs_ori} is the original observed data; n denotes the data points of each dataset) in the joint inversion. Considering the

Remote Sens. 2023, 15, 1730 5 of 16

teleseismic data have a good distribution on both the azimuthal and take-off angles of the source, and the InSAR data cover the entire coseismic deformation area well, we equally weighted the waveform data and deformation data in the inversion. Additionally, the relative weights of the teleseismic wave and InSAR deformation were set to 1. After the inversion, we shifted the teleseismic waves to best correlate their synthetics, because the teleseismic waves constrain only the relative position of fault slips compared with the hypocenter [27]. We used variance reduction (VR) to evaluate the data fitting by calculating as follows.

$$\begin{cases} VR_{i} = \left(1 - \frac{\sum_{n} (u^{obs}(n) - u^{syn}(n))^{2}}{\sum_{n} (u^{obs}(n))^{2}}\right) \\ VR_{Total} = \left(1 - \frac{\sum_{i=1}^{2} \sum_{n} (\lambda_{i} u_{i}^{obs}(n) - \lambda_{i} u_{i}^{syn}(n))^{2}}{\sum_{i=1}^{2} \sum_{n} (\lambda_{i} u_{i}^{obs}(n))^{2}}\right) \end{cases}$$
(2)

where the superscript 'obs' and 'syn' denote observed and synthetic data; λ_i is the relative weight corresponding to the i dataset; and the relative weights are set to 1 in this study.

3.2. Fault Geometry

The relocated aftershock distribution [21] delineates primarily a north-dipping segment $(60^{\circ}-65^{\circ})$ around the epicenter and a north-dipping ~75° dip angle on a fault segment along the Ravine du Sud fault (Figure 3b,c). The cross-section shows that the second and third segments have similar dip angles (Figure 3). The relocated aftershock distribution provides a prior reference for this fault system. Additionally, the rupture reached the surface from the T043A map (Figure 3a), which provides detailed information on the locations of the fault strike. Here, we constructed three fault segments for finite-fault inversion. Since the slip has not reached the surface around the epicenter, we determined the strike of the first segment using the grid-search method based on the finite-fault inversion. The uncertainty of the strike of the first segment needs to be considered, since less prior information can be used during the 2021 Haiti earthquake. The strike of the second segment is set 260° along the rupture traces, and the strike of the third segment is set 272° along the mapped Ravine du Sud fault (Figure 1a). Hence, the fault dips remained to be determined after fixing the strike. We grid-searched the optimal dip and strike of the first segment through the normalized misfit in finite-fault joint inversion. The dips of the second and third segments were assumed to be identical to improve the calculation efficiency in the finite-fault joint inversion. Finally, the optimal strike of the first segment is 269° (Figure 4a), which coincides with the non-linear inversion result [20]. The optimal dips of the first, second and third are 62°, 76° and 76°, respectively, corresponding to the minimum relative misfit of 0.22, and the result is consistent with the profile of the aftershock distribution (Figure 3c). The inferred fault geometry is illustrated in Figure 3d. Comparing the fault geometry derived from non-linear inversion using InSAR data only or aftershock distribution, the fault geometry derived from this study explained the teleseismic and InSAR data simultaneously, since we determined them based on the finite-fault joint inversion. The optimal fault geometry parameters of the three fault segments used in this study are listed in Table 1. Then, 645 subfaults were defined in rupture inversion and each subfault size is $2 \text{ km} \times 2 \text{ km}$. We used the epicentral location of 18.4°N , 73.5°W and the depth of 10 km as the rupture initiation point on the fault.

Table 1. Fault parameter setting of three fault segments.

	Strike/°	Dip/°	Length/km	Width/km
First segment	269	62	38	30
Second segment	260	76	18	30
Third segment	272	76	30	30

Remote Sens. 2023, 15, 1730 6 of 16

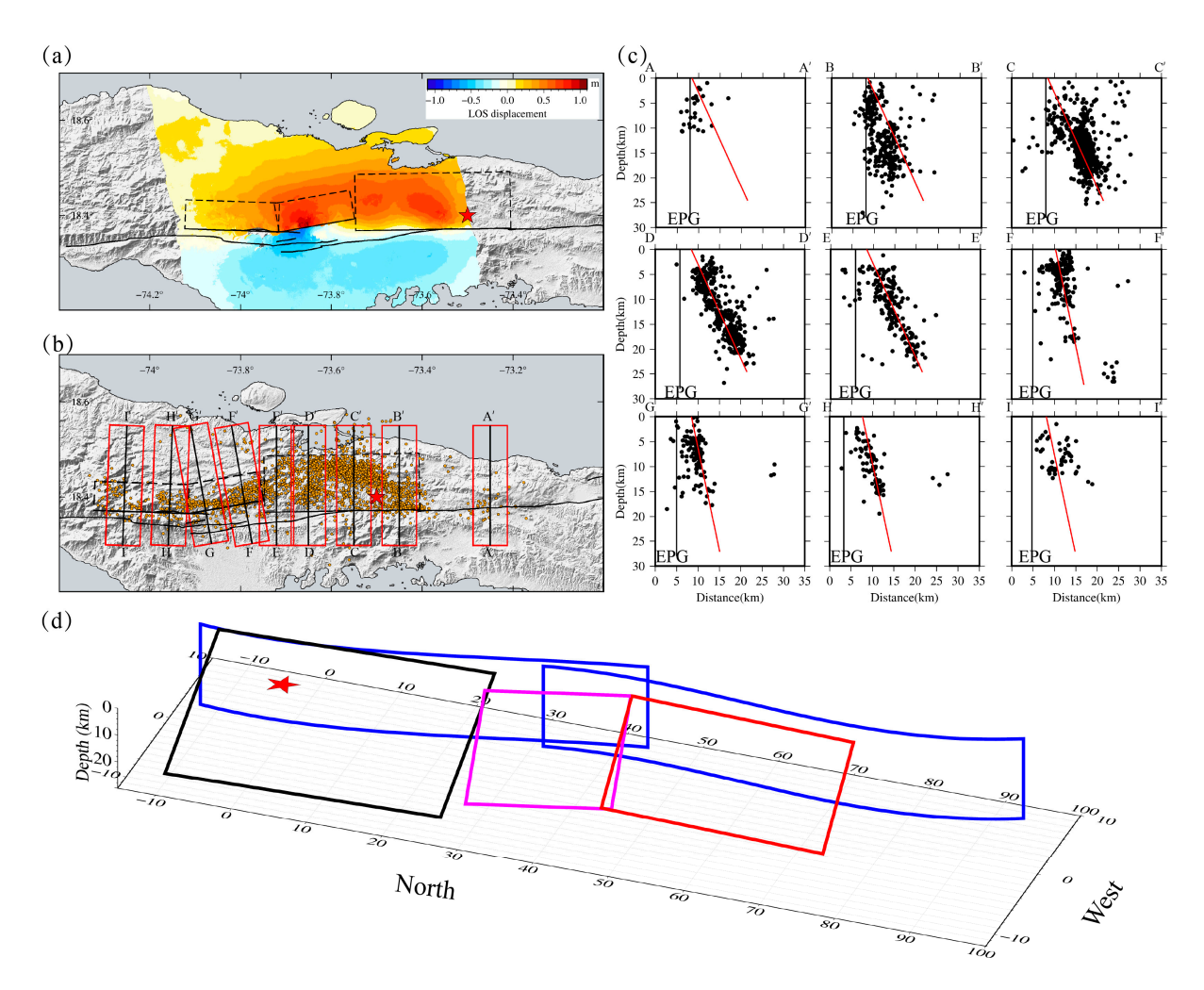


Figure 3. (a) Line-of-sight (LOS) displacement of T043A track and the projection of the fault geometry used in this study. (b) Orange dots denote the aftershock distribution, and hypocenters within the red rectangular box are projected into the corresponding north–south cross-section. (c) Aftershock distributions within different cross-sections; the vertical black lines mark the EPG fault; the red lines denote the inversion fault determined in our finite-fault inversion through the grid-search method. (d) View of the fault geometry model in 3D around the mainshock; the black, magenta and red rectangles denote the first, second and third faults used in this study. The blue rectangle denotes the EPG fault assumed to be purely vertical. The red star denotes the epicenter.

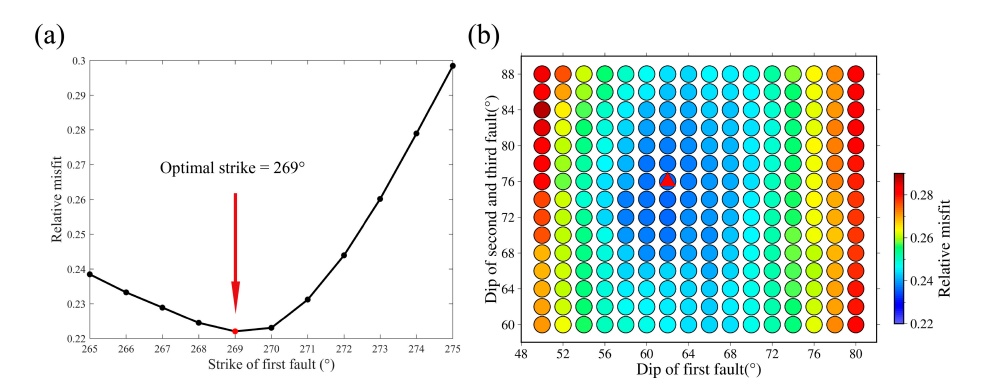


Figure 4. (a) Relative misfit plotted against different strikes with the first segment. Red circle denotes the optimal strike of 269°, corresponding to the minimum relative misfit of 0.22. (b) Relative misfit plotted against different dips with different fault segments; red triangle marks the minimum relative misfit with the different fault dips.

Remote Sens. 2023, 15, 1730 7 of 16

3.3. Results

Our finite-fault joint inversion results revealed a slip area about 65 km long and 25 km wide, and the 2021 Haiti earthquake ruptured unilaterally westward (Figures 5 and 6). Coseismic slip model and source time functions showed three slip patches: the first patch is centered near the epicenter in the first fault segment; the second patch is ~20 km west of the epicenter in the first fault segment; and the third slip patch is ~40 km west of the epicenter in the second fault segment (Figure 5b,c). The peak slips of the three slip patches are about 3.0 m, 2.3 m, and 2.8 m, respectively. The source time functions showed that the total rupture duration is 30 s, and the local peak moment rates appear at 7 s, 11 s, and 19 s, respectively. The total seismic moment is 7.93×10^{19} Nm, corresponding to the moment magnitude Mw7.2. For the first and second slip patches in the first segment fault, the slip was dominated by reverse motion, with little strike-slip motion. The average slip angle is ~60° in the first segment and decreases to ~25° in the second and third segments (Figure 5b). The coseismic slip distribution model shows that the slip has not reached the surface and is mainly concentrated at depths of 4-20 km in the first segment. In contrast, a shallow coseismic slip dominated by strike-slip motion reached the surface in the second segment fault, and the main slip was concentrated above 14 km depth, with the high-frequency signals derived by the slip reaching the surface captured using the back-projection method [18,20]. For the third segment, the slip is mainly concentrated at 6-10 km. The finite-fault model derived in this study shows that the rupture process is a combination of reverse motion around the epicenter and strike-slip motion to the west.

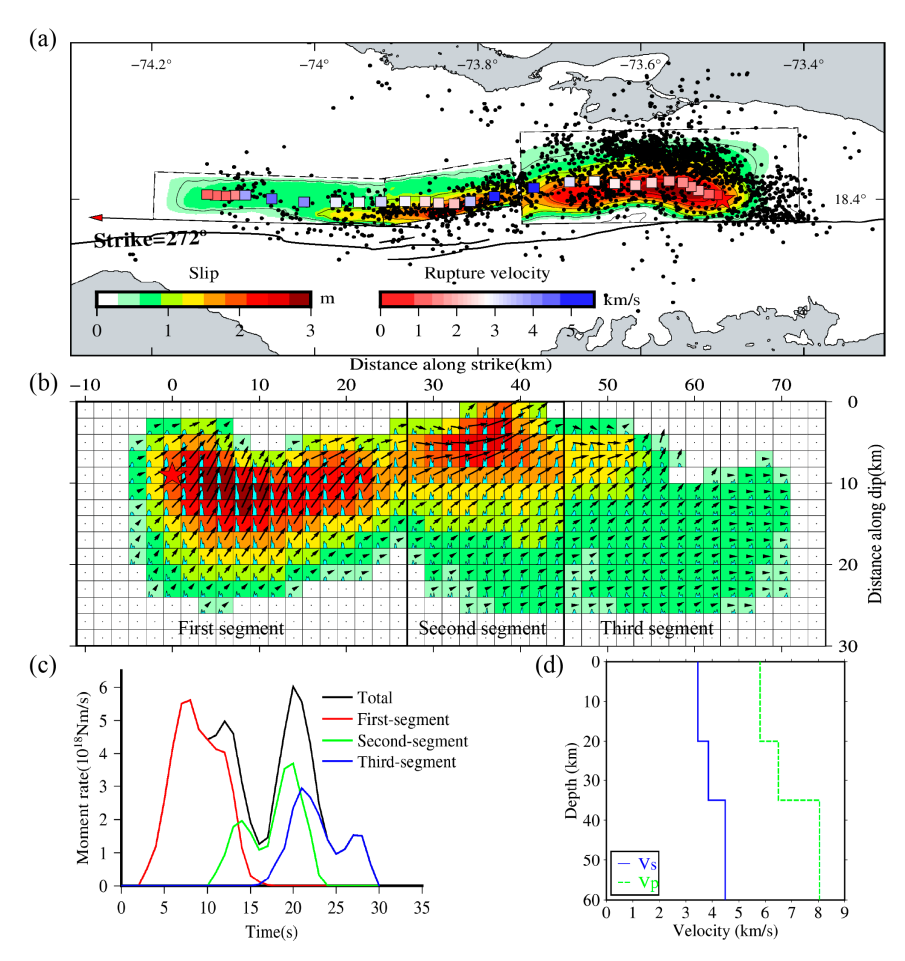


Figure 5. (a) Surface projection of the slip distributions from the finite-fault joint inversion and the centroid locations with every second and its centroid rupture velocity. Black dots denote the aftershock distributions. (b) Slip models from the joint inversion of the three segments. (c) Source time functions of the three fault segments. (d) AK135 velocity model used in this study.

Remote Sens. 2023, 15, 1730 8 of 16

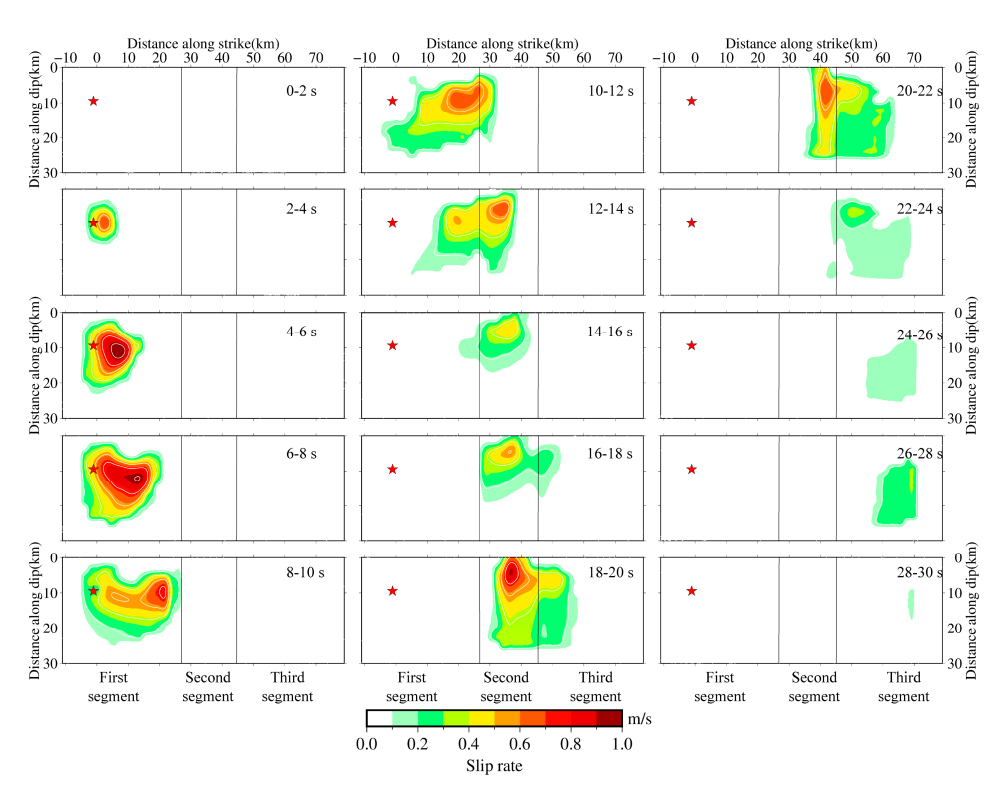


Figure 6. Temporal variations of the slip rate distribution of the three fault segments. Red star denotes the epicenter. The faults ruptured unilaterally, and the peak slip rate value is \sim 1.0 m/s. At \sim 10 s after the earthquake origin time, the second segment fault started to rupture, and at \sim 15 s the third segment fault started to rupture. The rupture of the first segment terminated at 20 s.

Figures 6 and S2 show the snapshots of the slip rate and slip distribution. In the first 6 s after earthquake initiation, the rupture expanded to a broad area along the fault and was mainly concentrated at depths of 4-20 km around the epicenter. At 6 s after earthquake initiation, the rupture propagated to the west, and at 10 s and 15 s, the second segment fault and third segment fault started to rupture, respectively (Figure 5c). At 10 s, the first segment fault released the most moment rate, and the rupture simultaneously jumped from a thrust event with a dip of 62° to a strike-slip event with a dip of 76°. The slips in the first slip patch and second slip patch terminated at 12 s and 16 s, respectively. We calculated the centroid rupture velocity by measuring the centroid speed, rather than the rupture-front velocity, because of the uncertainty of the estimation of the slip onset time for each subfault [31]. Figure 5a shows a significant abrupt change in rupture velocity at the junction between the first and second fault segments. Generally, slip migrating between different faults would cause an abrupt change in rupture velocity and/or slip rate [32–36]. Our results show that the rupture breaks through the stepover caused by the different fault geometry between the first and second segment faults and results in an abrupt change in rupture velocity. The centroid rupture velocity reached 4.6 km/s and 5.5 km/s at 13 s and 14 s, respectively. The interval of centroid location increases during the junction between the thrust and strike-slip fault (Figure 5a), and the temporal variations of the slip rate show a cascading rupture between the first and second fault segments (Figure 6). We also calculated the average rupture velocity based on the centroid rupture velocity. The result shows the average rupture velocity is approximately 2.6 km/s, similar to the back-projection [20] result (\sim 2.8–3.0 km/s).

The main difference in the rupture model between our study and previous studies may be dependent on the inversion data and inversion methods. A single dataset was used in the previous studies to determine the fault model, which will lead to the sparse spatial or temporal resolution. We also invert the rupture model using only teleseismic and InSAR data in this study. In our teleseismic slip model, two slip patches are consistently found:

Remote Sens. 2023, 15, 1730 9 of 16

the first slip patch is concentrated around the epicenter at the first segment, and the second slip patch is ~40 km west of the epicenter at the second segment (Figure S3 left panel). The teleseismic model appears to be smooth, most likely because of the poor resolution in spatial information of the teleseismic data. In contrast, three slip patches are identified in our InSAR data inversion (Figure S3 right panel). The InSAR model shows a higher spatial resolution than the teleseismic model. It is worth noting that the slip distribution derived from InSAR data is consistent with our joint inversion result because the near-field data constrain the absolute slip positions rather than the relative position compared with the hypocenter. A teleseismic waveform inversion study based on a potency-density tensor approach [37] in the 2021 Haiti earthquake found two major slip patches with a peak slip of 1.42 m: the first slip patch is centered near the epicenter, and the second slip patch is ~70 km west of the epicenter [18]. However, we found three slip patches in the InSAR model: the first is around the epicenter; the second is ~20 km west of the epicenter; and the third is ~40 km west of the epicenter. The major slip features (i.e., slip patches, scale) derived from the joint inversion are consistent with Calais et al. (2022) [20], because the InSAR data were used in the finite-fault inversion. The geodetic model based on InSAR data shows higher spatial resolution than teleseismic data inversion [19,20], while the geodetic model does not have temporal information about the earthquake. In summary, we built an improved rupture model of the 2021 Haiti earthquake that contains the spatiotemporal history by jointly inverting the teleseismic wave and InSAR deformation.

Comparisons between the observations and synthetics suggest that most of the observed data were well explained (Figure 7). The signal–noise ratio of the observed data, the crust velocity model, and the resolution ability of the data may influence the variance reduction value. In the inversion of the 2021 Haiti earthquake, teleseismic data show a low signal-to-noise ratio, and Green's function of teleseismic data only used AK135 velocity model, resulting in a lower variance reduction of 62.9%. However, the peak value of the teleseismic waves fit well (Figure 7a). The InSAR data fit well (Figure 7b) with a variance reduction of 92.5% because the surface deformation calculation is of higher accuracy.

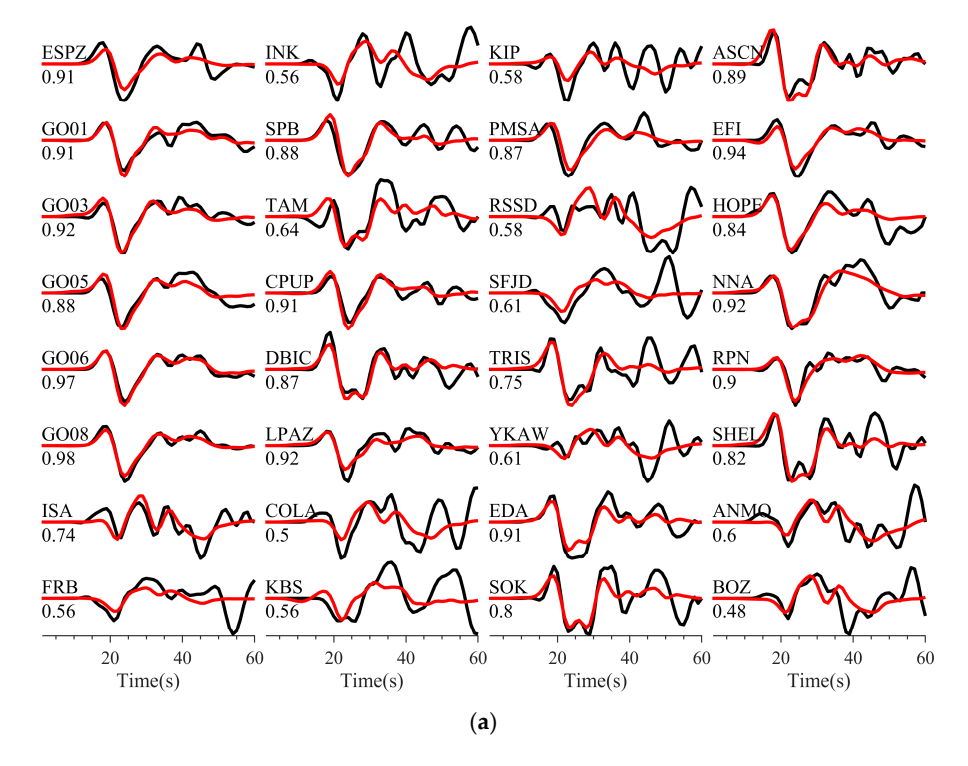


Figure 7. Cont.

Remote Sens. 2023, 15, 1730 10 of 16

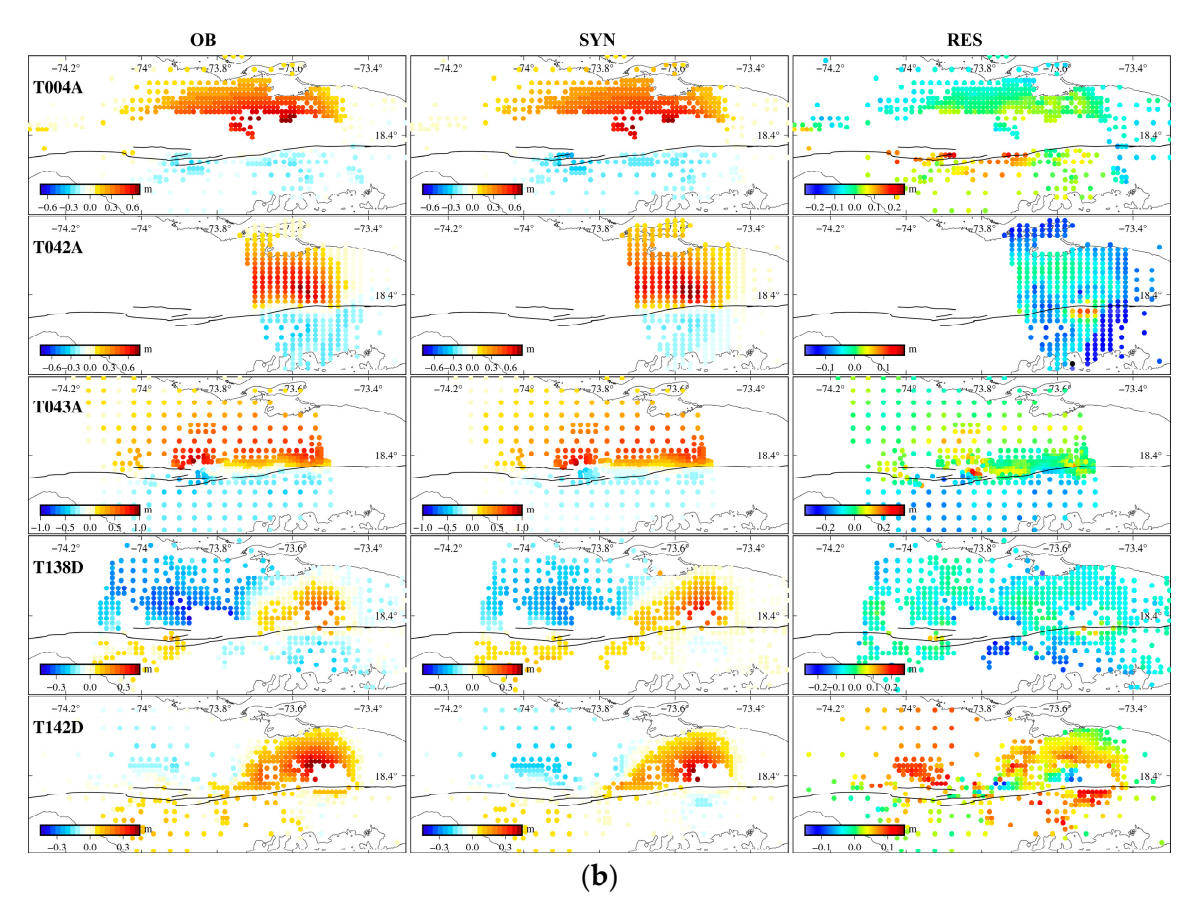


Figure 7. Comparison between the observed and synthesized data. (a) Teleseismic data fitting. The observed and synthesized waves in (a) are represented by black and red lines, respectively. The values denote the correlation coefficient between the observed and synthesized waves, and the teleseismic station names are given on the left-hand side of each figure. (b) InSAR data fitting. The first column denotes the observed data (OB); the second column denotes the synthetic data (SYN); and the third column denotes the residual between the observed and synthetic data (RES).

4. Discussion

4.1. Stability of the Rupture Model

To better illustrate the stability and effectiveness of the joint inversion, we performed a resolution test in this study (Figure 8). In the resolution test, we used a uniform rupture velocity of 2.5 km/s and a half-cycle triangle function with a length of 3 s to represent the source time function for each subfault. A single fault plane that is 86 km in length and 30 km in width with a strike of 270° and dip of 67° was used in the resolution test. The fault was divided into 645 subfaults, and each subfault size is 2 km \times 2 km. We assumed the epicenter is located at the 6th and 5th subfault in strike and dip direction, and three slip patches with slip values in each subfault are 3 m, with different depth extensions assumed in the input model (Figure 8c). We calculated the synthetic seismograms and synthetic surface deformation with the same data set (i.e., velocity model and observation dataset) used in the 2021 Haiti earthquake, according to the input slip model, and added 10 percent Gaussian noise. As mentioned previously, we used a maximum rupture velocity of 3 km/s and a duration time window of 8 s in the joint inversion after grid-search in the numerical experiments. Additionally, the fault strike and dip angles were allowed to change $\pm 5^{\circ}$ in the numerical experiments to test the resolution with different fault geometry parameters. It should be noted that synthetic data are more sensitive to strikes than dips: relative misfit changes more smoothly with various dip angles than with various strike angles (Figure 8a,b). However, we can still determine the optimal fault geometry parameters corresponding to the minimum relative misfit. The final strike and dip angles are 270° and

Remote Sens. 2023, 15, 1730 11 of 16

67°, respectively, corresponding to the relative misfit of 0.03. The fault geometry derived from the numerical tests is consistent with the input value (Figure 8), which means the fault geometry used in the real 2021 Haiti earthquake source inversion is reliable. To test the resolution with different data sets, we performed the finite-fault inversion using teleseismic data and InSAR data only. The slip model estimated from teleseismic data inversion only recovered two slip patches due to this low spatial resolution, and the maximum slip is slightly smaller than the input model (Figure 8d). For the InSAR data inversion, we noticed that the first and second slip patch cannot be well distinguished, and the peak value of the first and second is slightly smaller than the third slip patch. It should be because of its greater depth, and the InSAR data inversion always prefers to attribute the surface deformation to shallow-depth slip patches instead of the deep-depth slip patches (Figure 8e) [26]. Three slip patches are well retrieved by joint inversion and consistent with the input model (Figure 8f), indicating that joint inversion synthesizes the advantages of teleseismic data and InSAR data and results in an improved finite-fault model. Another factor that plays an important role in joint inversion is the relative weight of each data set. Because the teleseismic data and the InSAR data were normalized by their L^2 -norm and equally weighted in the joint inversion, the relative weights of the teleseismic data and InSAR data are set to 1. The numerical experiment indicates that the joint inversion has improved the resolution of the slip model on the slip distribution, scale and maximum slip values. The joint inversion combines the advantages of teleseismic inversion and geodetic inversion, suggesting that the model derived from joint inversion is reliable.

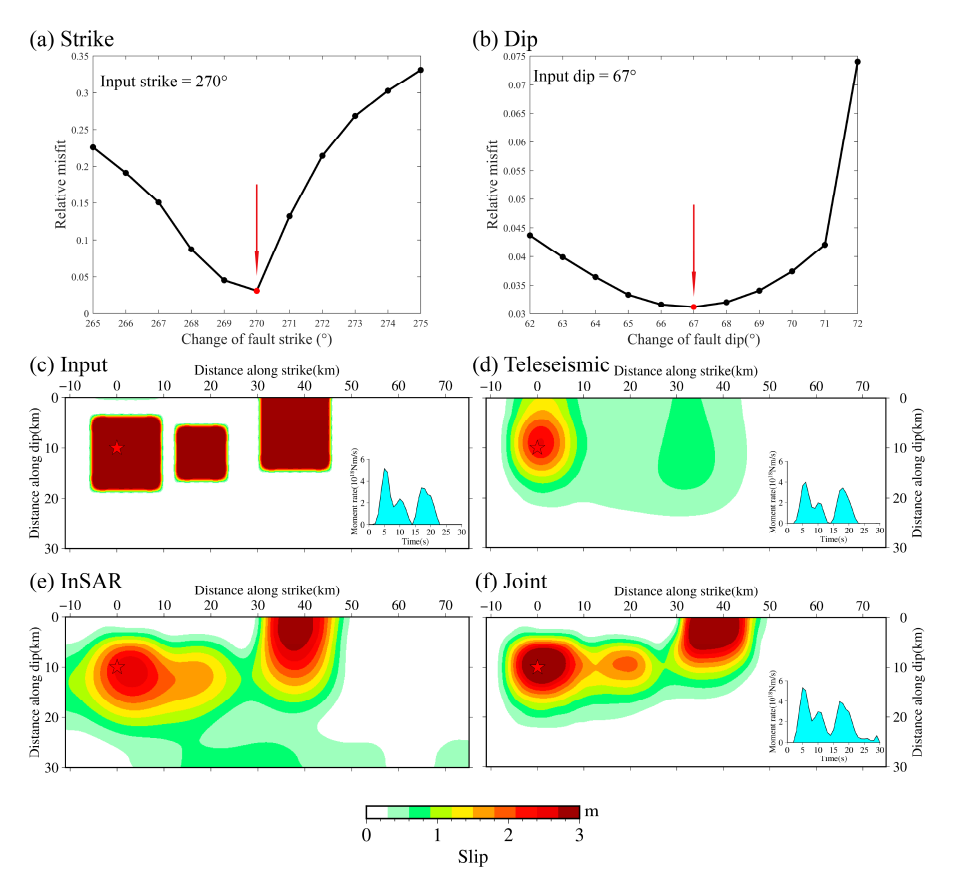


Figure 8. Resolution test. The strike and dip in input model are 270° and 67° , respectively. (a) Relative misfit plotted against different strike angles. (b) Relative misfit plotted against different dip angles. Red circles in (\mathbf{a},\mathbf{b}) denote the optimal strike of 270° and the optimal dip of 67° , corresponding to the minimum relative misfit of 0.03. (c) Given slip model with three slip patches. (d) Slip model from the teleseismic data inversion. (e) Slip model from the geodetic InSAR data inversion. (f) Slip model from the joint inversion. Source time functions are shown in the bottom right corner in $(\mathbf{c},\mathbf{d},\mathbf{f})$. The red star in $(\mathbf{c}-\mathbf{f})$ denotes the pricenter, the source time function is showed in the right bottom with cyan.

Remote Sens. 2023, 15, 1730 12 of 16

4.2. Cascading Rupture of the Multi-Fault System

Our preferred rupture model shows that the rupture is initiated at a fault dominated by reverse motion and jumps to a fault dominated by strike-slip motion. As shown in Figure 8a, the strikes of the first, second and third fault segments used in this study are 269°, 260°, and 272°, respectively, and the dips are 62°, 76°, 76°, respectively. These strike and dip angle changes can act as a geometric barrier that was caused by the irregular fault geometry between the multi-fault segments of the 2021 Haiti earthquake. The rupture process of the 2021 Haiti main shock indicates the rupture broke through the stepover, causing a simultaneous rupture process and a cascade rupture scenario between the first and second fault segments (Figure 6). Figure 4a shows the abrupt change in rupture velocity around the junction between the thrust and strike-slip fault, with the maximum centroid rupture velocity of ~5.5 km/s, coinciding with the migration speed of 6 km/s in Okuwaki and Fan (2022). It is noted that many other factors, including hypocenter location and extra near-field observed data, will influence the centroid rupture velocity calculation and are needed in future work to reveal more detailed rupture kinematics. In the case of the 2021 Haiti earthquake, the rupture broke through the stepover during the major earthquake, causing a cascade rupture and fast rupture propagation.

The 2021 Haiti earthquake has many similarities with the 2010 event in southern Haiti. Both earthquakes initiated with a reverse motion on an eastern segment and propagated to the west with the strike-slip motion [12,13]. The oblique plate convergence may explain such a multi-fault rupture process combining reverse motion and strikeslip motion. The 2021 Haiti earthquake was also consistent with the 2002 Mw7.9 Denali, Alaska, earthquake [38], the 2003 Mw6.6 Bam, Iran, earthquake [39], and the 2008 Mw7.9 Wenchuan, China, earthquake [40,41], with the rupture processes including simultaneous or near-simultaneous reverse and strike-slip motion. An earthquake with a simultaneous multi-fault rupture often leads to higher hazards [42] because breaking through multiple segments may require critically loaded faults, leading to the release of large stress accumulations [41]. The 2021 Haiti earthquake broke through the stepover that connects the first and second segments in a cascade rupture. The cascade rupture scenario may help explain why most of the landslides occurred in the west compared to the epicenter, especially in the Pic Macaya National Park, where the terrain is rugged [24]. Our rupture model shows the 2021 Haiti earthquake propagated unilaterally from east to west, and the slip reached the surface close to the Pic Macaya National Park. Areas toward the rupture direction experience a directivity pulse of high ground motions, and the rupture front bears high amplitudes and short duration; this Doppler effect in the 2021 Haiti earthquake may be an additional factor explaining the many landslides concentrated in the west compared to the epicenter [24,43].

4.3. Potential Seismic Hazard

Southern Haiti, controlled by complex seismotectonic structures, shows high seismic hazards. Many studies have demonstrated that the Δ CFS values associated with an earthquake can induce or retard seismic activities in the peripheral fault zone. Calculations of the Δ CFS associated with earthquake failure have been used to explain seismic observations, including aftershock distributions, in normally active regions following large earthquakes [44–47]. Moreover, the failure threshold for inducing or delaying the occurrence of an earthquake is considered to be ± 0.01 MPa [47]. It should be noted that Coulomb stress disturbances do not change the nature of regional strain accumulation but rather advance or delay the time of earthquake occurrence [48]. Previous studies show that the 2010 earthquake triggered the 2021 earthquake: the initiation area of the 2021 rupture occurred in regions that the Δ CFS calculated to have been brought to >0.01 MPa (or 0.1 Bar) (called stress triggering zone) caused by 2010 events [18,20,49]. In this study, we calculated the influence of the Δ CFS caused by the 2021 Haiti earthquake on the surrounding fault zone based on the coseismic slip model derived from our joint inversion. We evaluated the Δ CFS using Coulomb 3.4 [50,51] at a depth of 20 km, since most aftershocks occurred

Remote Sens. 2023, 15, 1730 13 of 16

at 15–20 km (Figure 9a, inset in the upper left), and the effective friction coefficient was set to 0.4. Figure 9a shows that most aftershocks occurred in stress-triggering zones, and the cross-section of a-a' (Figure 9a, inset in the bottom right) shows that most aftershocks occurred at shallow depths (about >12 km), corresponding to the Δ CFS distribution on the EPG fault (Figure 9b).

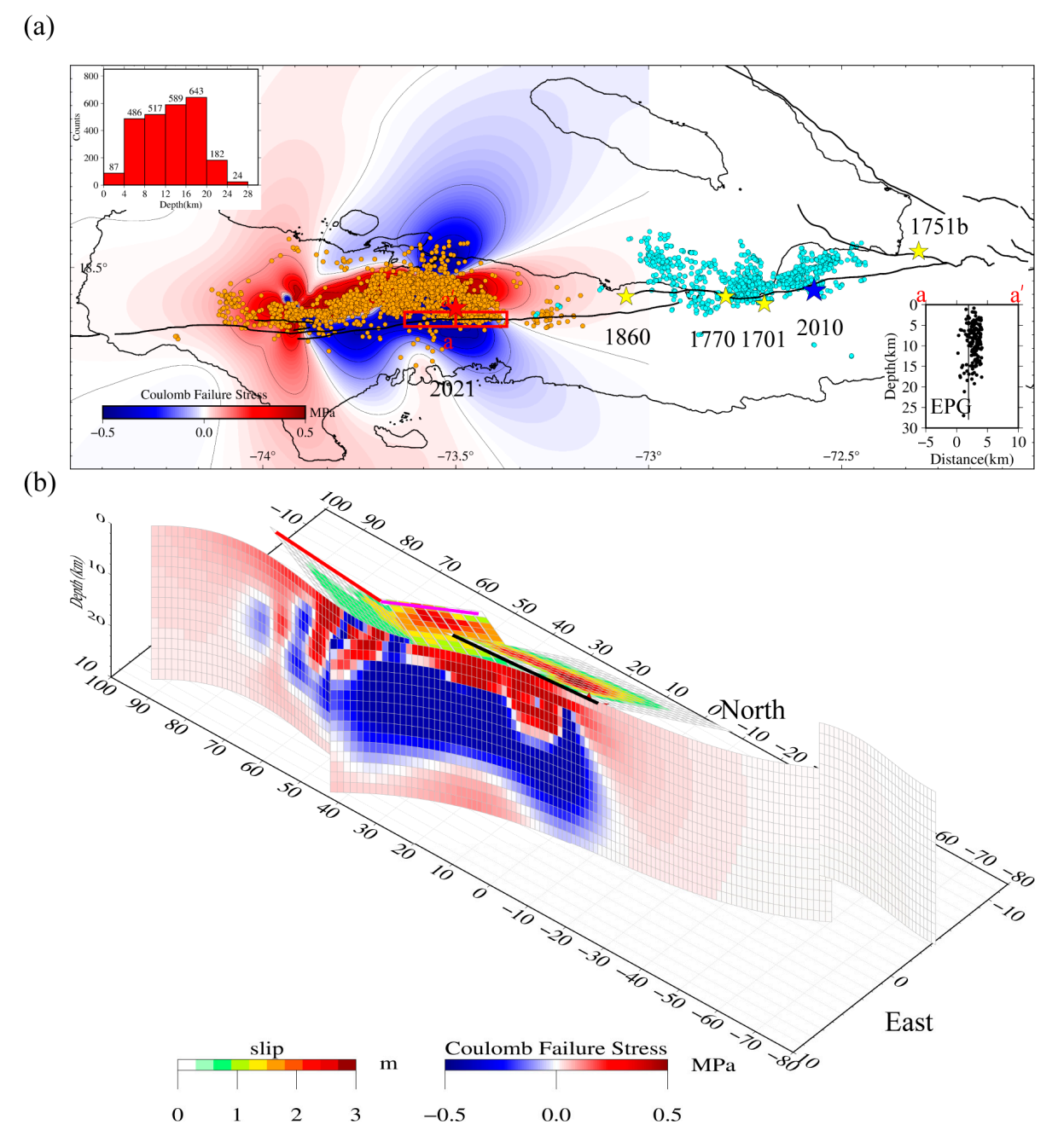


Figure 9. (a) Coulomb stresses calculated at a depth of 20 km using the source model derived in this study. The EPG fault is set along with the fault trace, the dip angle is set to 90°, and the rake angle is set as pure left-lateral strike-slip. The red, blue and yellow stars denote the epicenter location of 2021, 2010 and historic earthquakes. The orange dots denote the relocated aftershock catalogs from 20 August to 31 December 2021; the cyan dots denote the relocated aftershock catalogs after the 2010 main shock. The statistics of aftershock with different depths are showed in the upper left. (b) Coulomb stresses resolved on simplified planes and the coseismic slip model.

Remote Sens. 2023, 15, 1730 14 of 16

The non-rupture of the 70 km long segment directly adjacent to the 2010 earthquake may be explained by the fact that this region could have ruptured prehistorically [49]. Stress released in the 1770 earthquake maybe have been rebuilt by the 2010 earthquake, and additional stress caused by the 2010 event may have advanced the occurrence of the 2021 earthquake [49]. The historic earthquake studies show that the 1770 earthquake was a major event with Mw7.5 or larger; the combined moment release of the 2010 and 2021 earthquakes is commensurate with an Mw7.3 earthquake, smaller than the 1770 earthquake [10,11]. The 1860 earthquake is inferred to have released strain in the gap between the 2010 and 2021 events [10]; the stress released in the 1860 earthquake may have rebuilt, and we cannot rule out the possibility of the earthquake rupture in the gap between 2010 and 2021 events. Our result shows that the west of the 2021 main shock and the gap between the 2010 and 2021 earthquakes are located in the stress-trigging zone caused by the 2021 earthquake. This result indicates that the possibility of earthquakes occurring to the west and east of the 2021 main shock cannot be ignored.

5. Conclusions

In this study, we imaged the kinematic rupture process with three fault segments of the 2021 Haiti earthquake using teleseismic and InSAR data, and we determined the fault dips through the grid-search method in joint inversion. Our results indicate the following: (1) The first, second and third fault dips are 62°, 76° and 76°, respectively. Three slip patches were clearly distinguished in our preferred model. The main slip of the first and second slip patches was dominated by the reverse motion, and the third slip patch was dominated by the strike-slip motion. (2) This rupture process likely results from the oblique convergence between the Caribbean and Gonave microplate. The earthquake initiated at a fault dominated by reverse motion and jumped to a fault dominated by strike-slip motion. (3) The rupture broke through the stepover, causing a cascading rupture and abrupt change in rupture velocity between the junction of the thrust and strike-slip fault segment. (4) Most landslides occurred at the west of the epicenter due to the Doppler effects and the high rupture velocity feature from east to west in this unilateral rupture earthquake. In addition, based on a Coulomb stress analysis and historic earthquake studies, we postulate that future earthquakes may occur to the west and east of the 2021 Haiti mainshock, and we cannot rule out the possibility that the EPG fault could rupture.

Supplementary Materials: The following supporting information can be downloaded at: https://www.mdpi.com/article/10.3390/rs15071730/s1, (1) Figure S1 showing the LOS displacement of the five tracks, (2) Figure S2 showing temporal variations of the slip distribution in three-segment fault from the finite-fault joint inversion, (3) Figure S3 showing slip models from the inversions of the teleseismic data and InSAR data only.

Author Contributions: Conceptualization, G.W., X.L. and Y.Z. (Yong Zhang); Data curation, G.W. and Y.Z. (Yingwen Zhao); Investigation, G.W. and X.L.; Methodology, G.W., X.L. and Y.Z. (Yong Zhang); Validation, X.L., Y.Z. (Yong Zhang) and C.X.; Writing—original draft, G.W., X.L., Y.Z. (Yong Zhang), Y.Z. (Yingwen Zhao) and Y.Z. (Yuxin Zheng); Writing—review and editing, G.W., X.L., Y.Z. (Yong Zhang), C.X., Y.Z. (Yingwen Zhao) and Y.Z. (Yuxin Zheng). All authors have read and agreed to the published version of the manuscript.

Funding: This research was funded by the National Natural Science Foundation of China (No. 41974027), the National Key R&D Program of China (2021YFC3000504), the Hubei Province Natural Science Foundation (Grant No. 2020CFA002), and the Sino-German Mobility Programme (Grant No. M-0054).

Data Availability Statement: The teleseismic data were downloaded from the IRIS Wilber 3 system (http://ds.iris.edu/wilber3/find_event, accessed on 10 May 2022). The InSAR data were downloaded from Yin et al. (2022) (https://topex.ucsd.edu/haiti_7.2/index.html, accessed on 21 November 2022). The focal mechanisms were available from the U.S. Geological Survey (USGS; https://earthquake.usgs.gov/earthquakes/eventpage, accessed on 20 August 2021), Global Centroid Moment Tensor (GCMT; https://www.globalcmt.org/CMTsearch.html, accessed on 25 August 2021). Relocated

Remote Sens. 2023, 15, 1730 15 of 16

aftershock hypocenters were available from the supplements of Douilly et al. (2022) (https://pubs.geoscienceworld.org/ssa/bssa/article/doi/10.1785/0120220128/618187/Rupture-Segmentation-of-the-14-August-2021-Mw-7-2, accessed on 10 December 2022). Maps were made using the Generic Mapping Tools program (https://www.generic-mapping-tools.org/, accessed on 15 March 2022).

Acknowledgments: The authors would like to acknowledge the reviewers for their comments and suggestions, which help in improving the quality of the manuscript.

Conflicts of Interest: The authors declare no conflict of interest.

References

- UN Office for the Coordination of Humanitarian Affairs (UN-OCHA). Haiti: Earthquake Situation Report No. 8—Final (29 November 2021). ReliefWeb, 2021. Available online: https://reliefweb.int/report/haiti/haiti-earthquake-situation-report-no-8-final-29-november-2021 (accessed on 10 December 2021).
- 2. Manaker, D.M.; Calais, E.; Freed, A.M.; Ali, S.T.; Przybylski, P.; Mattioli, G.; Jansma, P.; Prépetit, C.; De Chabalier, J.B. Interseismic Plate coupling and strain partitioning in the Northeastern Caribbean. *Geophys. J. Int.* 2008, 174, 889–903. [CrossRef]
- 3. Benford, B.; DeMets, C.; Calais, E. GPS estimates of microplate motions, northern Caribbean: Evidence for a Hispaniola microplate and implications for earthquake hazard. *Geophys. J. Int.* **2012**, *191*, 481–490. [CrossRef]
- 4. Fleur, N.S.; Feuillet, N.; Grandin, R.; Jacques, E.; Weil-Accardo, J.; Klinger, Y. Seismotectonics of southern Haiti: A new faulting model for the 12 January 2010 M 7.0 earthquake. *Geophys. Res. Lett.* 2015, 42, 10273–10281. [CrossRef]
- 5. Calais, É.; Symithe, S.; de Lépinay, B.M.; Prépetit, C. Plate boundary segmentation in the northeastern Caribbean from geodetic measurements and Neogene geological observations. *C. R. Geosci.* **2016**, *348*, 42–51. [CrossRef]
- 6. Mann, P.; Burke, K.; Matumoto, T. Neotectonics of Hispaniola: Plate motion, sedimentation, and seismicity at a restraining bend. *Earth Planet. Sci. Lett.* **1984**, 70, 311–324. [CrossRef]
- 7. Prentice, C.S.; Mann, P.; Crone, A.J.; Gold, R.D.; Hudnut, K.W.; Briggs, R.W.; Koehler, R.D.; Jean, P. Seismic hazard of the Enriquillo–Plantain Garden fault in Haiti inferred from palaeoseismology. *Nat. Geosci.* **2010**, *3*, 789–793. [CrossRef]
- 8. Symithe, S.; Calais, E. Present-day shortening in Southern Haiti from GPS measurements and implications for seismic hazard. *Tectonophysics* **2016**, *679*, 117–124. [CrossRef]
- 9. Bakun, W.H.; Flores, C.; Brink, U.S.T. Significant earthquakes on the Enriquillo fault system, hispaniola, 1500–2010: Implications for seismic hazard. *Bull. Seismol. Soc. Am.* **2012**, 102, 18–30. [CrossRef]
- 10. Martin, S.S.; Hough, S.E. The 8 April 1860 Jour de Pâques earthquake sequence in southern Haiti. *Bull. Seismol. Soc. Am.* **2022**, 112, 2468–2486. [CrossRef]
- 11. Hough, S.E.; Martin, S.S.; Symithe, S.J.; Briggs, R. Rupture Scenarios for the 3 June 1770 Haiti Earthquake. *Bull. Seismol. Soc. Am.* **2022**, *113*, 157–185. [CrossRef]
- 12. Hayes, G.P.; Briggs, R.W.; Sladen, A.; Fielding, E.J.; Prentice, C.; Hudnut, K.; Mann, P.; Taylor, F.W.; Crone, A.J.; Gold, R.; et al. Complex rupture during the 12 January 2010 Haiti earthquake. *Nat. Geosci.* **2010**, *3*, 800–805. [CrossRef]
- 13. Calais, E.; Freed, A.; Mattioli, G.; Amelung, F.; Jónsson, S.; Jansma, P.; Hong, S.-H.; Dixon, T.; Prépetit, C.; Momplaisir, R. Transpressional rupture of an unmapped fault during the 2010 Haiti earthquake. *Nat. Geosci.* **2010**, *3*, 794–799. [CrossRef]
- 14. Douilly, R.; Haase, J.S.; Ellsworth, W.; Bouin, M.-P.; Calais, E.; Symithe, S.; Armbruster, J.G.; De Lépinay, B.M.; Deschamps, A.; Mildor, S.-L.; et al. Crustal Structure and Fault Geometry of the 2010 Haiti Earthquake from Temporary Seismometer Deployments. *Bull. Seismol. Soc. Am.* 2013, 103, 2305–2325. [CrossRef]
- 15. Symithe, S.J.; Calais, E.; Haase, J.S.; Freed, A.M.; Douilly, R. Coseismic Slip Distribution of the 2010 M 7.0 Haiti Earthquake and Resulting Stress Changes on Regional Faults. *Bull. Seismol. Soc. Am.* **2013**, 103, 2326–2343. [CrossRef]
- 16. Geospatial Information Authority of Japan. The 2021 Haiti Earthquake: Crustal Deformation Detected by ALOS-2 Data. 2021. Available online: https://www.gsi.go.jp/cais/topic20210814-e.html (accessed on 10 December 2021).
- 17. Yin, H.Z.; Xu, X.; Haase, J.S.; Douilly, R.; Sandwell, D.T.; de Lepinay, B.M. Surface Deformation Surrounding the 2021 Mw 7.2 Haiti Earthquake Illuminated by InSAR Observations. *Bull. Seismol. Soc. Am.* 2022, 113, 41–57. [CrossRef]
- 18. Okuwaki, R.; Fan, W. Oblique Convergence Causes Both Thrust and Strike-Slip Ruptures during the 2021 M 7.2 Haiti Earthquake. *Geophys. Res. Lett.* **2022**, 49, e2021GL096373. [CrossRef]
- 19. Maurer, J.; Dutta, R.; Vernon, A.; Vajedian, S. Complex Rupture and Triggered Aseismic Creep during the 14 August 2021 Haiti Earthquake from Satellite Geodesy. *Geophys. Res. Lett.* 2022, 49, e2022GL098573. [CrossRef]
- 20. Calais, E.; Symithe, S.; Monfret, T.; Delouis, B.; Lomax, A.; Courboulex, F.; Ampuero, J.P.; Lara, P.E.; Bletery, Q.; Chèze, J.; et al. Citizen seismology helps decipher the 2021 Haiti earthquake. *Science* **2022**, *376*, 283–287. [CrossRef]
- 21. Douilly, R.; Paul, S.; Monfret, T.; Deschamps, A.; Ambrois, D.; Symithe, S.J.; Fleur, S.S.; Courboulex, F.; Calais, E.; Boisson, D.; et al. Rupture Segmentation of the 14 August 2021 Mw 7.2 Nippes, Haiti, Earthquake Using Aftershock Relocation from a Local Seismic Deployment. *Bull. Seismol. Soc. Am.* 2022, 113, 58–72. [CrossRef]
- 22. Fleur, N.S.; Klinger, Y.; Feuillet, N. Detailed map, displacement, paleoseismology, and segmentation of the Enriquillo-Plantain Garden Fault in Haiti. *Tectonophysics* **2020**, *778*, 228368. [CrossRef]
- 23. Styron, R.; García-Pelaez, J.; Pagani, M. CCAF-DB: The Caribbean and Central American active fault database. *Nat. Hazards Earth Syst. Sci.* **2020**, 20, 831–857. [CrossRef]

Remote Sens. 2023, 15, 1730 16 of 16

24. Martinez, S.N.; Allstadt, K.E.; Slaughter, S.L.; Schmitt, R.G.; Collins, E.; Schaefer, L.N.; Ellison, S. *Landslides Triggered by the August* 14, 2021, *Magnitude 7.2 Nippes, Haiti, Earthquake (No. 2021-1112)*; U.S. Geological Survey: Reston, VA, USA, 2021. [CrossRef]

- 25. Jonsson, S. Fault Slip Distribution of the 1999 Mw 7.1 Hector Mine, California, Earthquake, Estimated from Satellite Radar and GPS Measurements. *Bull. Seismol. Soc. Am.* **2002**, 92, 1377–1389. [CrossRef]
- 26. Zhang, Y.; Feng, W.; Chen, Y.; Xu, L.; Li, Z.; Forrest, D. The 2009 L'Aquila MW 6.3 earthquake: A new technique to locate the hypocentre in the joint inversion of earthquake rupture process. *Geophys. J. Int.* 2012, 191, 1417–1426. [CrossRef]
- 27. Zhang, Y.; Feng, W.; Li, X.; Liu, Y.; Ning, J.; Huang, Q. Joint Inversion of Rupture across a Fault Stepover during the 8 August 2017 Mw 6.5 Jiuzhaigou, China, Earthquake. *Seism. Res. Lett.* **2021**, 92, 3386–3397. [CrossRef]
- 28. Wang, R.; Heimann, S.; Zhang, Y.; Wang, H.; Dahm, T. Complete synthetic seismograms based on a spherical self-gravitating Earth model with an atmosphere–ocean–mantle–core structure. *Geophys. J. Int.* **2017**, 210, 1739–1764. [CrossRef]
- 29. Kennett, B.L.N.; Engdahl, E.R.; Buland, R. Constraints on seismic velocities in the Earth from traveltimes. *Geophys. J. Int.* **1995**, 122, 108–124. [CrossRef]
- 30. Wang, R.; Lorenzo-Martín, F.; Roth, F. PSGRN/PSCMP—A new code for calculating co- and post-seismic deformation, geoid and gravity changes based on the viscoelastic-gravitational dislocation theory. *Comput. Geosci.* **2006**, *32*, 527–541. [CrossRef]
- 31. Xu, Y.; Zhang, Y.; Xu, L. Geometry-dependent rupture process of the 2015 Gorkha, Nepal, earthquake determined using a dip-varying inversion approach with teleseismic, high-rate GPS, static GPS and InSAR data. *Geophys. J. Int.* **2021**, 229, 1408–1421. [CrossRef]
- 32. Aki, K. Characterization of barriers on an earthquake fault. J. Geophys. Res. Atmos. 1979, 84, 6140–6148. [CrossRef]
- 33. Kase, Y.; Day, S.M. Spontaneous rupture processes on a bending fault. Geophys. Res. Lett. 2006, 33. [CrossRef]
- 34. Madariaga, R.; Ampuero, J.P.; Adda-Bedia, M. Seismic radiation from simple models of earthquakes. *Geophys. Monogr.* **2006**, 170, 223–236. [CrossRef]
- 35. Bruhat, L.; Fang, Z.; Dunham, E.M. Rupture complexity and the supershear transition on rough faults. *J. Geophys. Res. Solid Earth* **2016**, 121, 210–224. [CrossRef]
- 36. Okuwaki, R.; Yagi, Y. Role of geometric barriers in irregular-rupture evolution during the 2008 Wenchuan earthquake. *Geophys. J. Int.* 2017, 212, 1657–1664. [CrossRef]
- 37. Shimizu, K.; Yagi, Y.; Okuwaki, R.; Fukahata, Y. Development of an inversion method to extract information on fault geometry from teleseismic data. *Geophys. J. Int.* **2020**, 220, 1055–1065. [CrossRef]
- Aagaard, B.T. Dynamic Rupture Modeling of the Transition from Thrust to Strike-Slip Motion in the 2002 Denali Fault Earthquake, Alaska. Bull. Seismol. Soc. Am. 2004, 94, S190–S201. [CrossRef]
- 39. Talebian, M.; Fielding, E.J.; Funning, G.J.; Ghorashi, M.; Jackson, J.; Nazari, H.; Parsons, B.; Priestley, K.; Rosen, P.A.; Walker, R.; et al. The 2003 Bam (Iran) earthquake: Rupture of a blind strike-slip fault. *Geophys. Res. Lett.* **2004**, *31*. [CrossRef]
- 40. Liu-Zeng, J.; Zhang, Z.; Wen, L.; Tapponnier, P.; Sun, J.; Xing, X.; Hu, G.; Xu, Q.; Zeng, L.; Ding, L.; et al. Co-seismic ruptures of the 12 May 2008, Ms 8.0 Wenchuan earthquake, Sichuan: East–west crustal shortening on oblique, parallel thrusts along the eastern edge of Tibet. *Earth Planet. Sci. Lett.* 2009, 286, 355–370. [CrossRef]
- 41. Shen, Z.-K.; Sun, J.; Zhang, P.; Wan, Y.; Wang, M.; Burgmann, R.; Zeng, Y.; Gan, W.; Liao, H.; Wang, Q. Slip maxima at fault junctions and rupturing of barriers during the 2008 Wenchuan earthquake. *Nat. Geosci.* 2009, 2, 718–724. [CrossRef]
- 42. Walters, R.J.; Gregory, L.C.; Wedmore, L.N.J.; Craig, T.J.; McCaffrey, K.; Wilkinson, M.; Chen, J.; Li, Z.; Elliott, J.R.; Goodall, H.; et al. Dual control of fault intersections on stop-start rupture in the 2016 Central Italy seismic sequence. *Earth Planet. Sci. Lett.* **2018**, 500, 1–14. [CrossRef]
- 43. Somerville, P.G.; Smith, N.F.; Graves, R.W.; Abrahamson, N.A. Modification of Empirical Strong Ground Motion Attenuation Relations to Include the Amplitude and Duration Effects of Rupture Directivity. *Seism. Res. Lett.* **1997**, *68*, 199–222. [CrossRef]
- 44. Stein, R.S. The role of stress transfer in earthquake occurrence. Nature 1999, 402, 605–609. [CrossRef]
- 45. Freed, A.M. Earthquake triggering by static, dynamic, and postseismic stress transfer. *Annu. Rev. Earth Planet. Sci.* **2005**, *33*, 335–367. [CrossRef]
- 46. Nalbant, S.S.; McCloskey, J. Stress evolution before and after the 2008 Wenchuan, China earthquake. *Earth Planet. Sci. Lett.* **2011**, 307, 222–232. [CrossRef]
- 47. Toda, S.; Stein, R.S. Long- and Short-Term Stress Interaction of the 2019 Ridgecrest Sequence and Coulomb-Based Earthquake Forecasts. *Bull. Seismol. Soc. Am.* **2020**, *110*, 1765–1780. [CrossRef]
- 48. He, K.; Wen, Y.; Xu, C.; Zhao, Y. Fault Geometry and Slip Distribution of the 2021 Mw 7.4 Maduo, China, Earthquake Inferred from InSAR Measurements and Relocated Aftershocks. *Seism. Res. Lett.* **2021**, *93*, 8–20. [CrossRef]
- 49. Stein, R.; Temblor; Toda, S.; Lin, J.; Sevilgen, V. *Are the 2021 and 2010 Haiti Earthquakes Part of a Progressive Sequence?* Temblor: Redwood City, CA, USA, 2021. [CrossRef]
- 50. Toda, S.; Stein, R.S.; Richards-Dinger, K.; Bozkurt, S.B. Forecasting the evolution of seismicity in southern California: Animations built on earthquake stress transfer. *J. Geophys. Res. Atmos.* **2005**, *110*. [CrossRef]
- 51. Lin, J.; Stein, R.S. Stress triggering in thrust and subduction earthquakes and stress interaction between the southern San Andreas and nearby thrust and strike-slip faults. *J. Geophys. Res. Solid Earth* **2004**, *109*. [CrossRef]

Disclaimer/Publisher's Note: The statements, opinions and data contained in all publications are solely those of the individual author(s) and contributor(s) and not of MDPI and/or the editor(s). MDPI and/or the editor(s) disclaim responsibility for any injury to people or property resulting from any ideas, methods, instructions or products referred to in the content.